Hall Sensor based Transnational and Rotary Position Sensing System

Ye gu Kang, *Member, IEEE,* Daniel Fernandez, *Member, IEEE,*

***Abstract*—This paper presents a new methodology to determine both rotary and translational positions required for a magnetic levitation system and robot joint. Permanent magnets are mounted on the moving part while the low-cost hall-effect sensors are measuring radial direction magnetic flux on the stationary part. Hall sensors are strategically placed to enable use of differential information. The radial flux are post-processed for position estimation without filter; only addition and multiplication operations are required. Vertical and horizontal position displacement induced zero-sequences from Clark' transformation are used; differential information enables translational and rotary position estimation. The manufactured sensor's rotary position range is 0 to 2π and the translation position range is within 1mm in both x- and y-axes from the center position. The proposed sensing system is a low-cost, compact in size.**

***Index Terms*—Hall effect sensor, Magnetic levitation, Position sensor, Rotary position, Self-bearing machine, Transnational position, Zero-sequence.**

I. Introduction

MAGNETIC levitation systems require both translational and rotary position information, i.e., x, y, and θ_r, as shown in Fig. 1; x- and y-axes being horizontal and vertical axes, and rotary position, θ_r [1].

xy-position sensors for levitation system position control can be classified into: eddy current based [1], inductance or capacitance based[], hall effect based [2], [3], and optical based sensors [4], [5]. Eddy current or inductance based sensor are relatively expensive since they require excitation and signal-processing system. Optical based sensor should prevent optical blockage and reflection on the surface. Hall sensors are the cheapest and compact in size. All these sensors result in additional volume, cost [4], [6] and frequently represent a large amount of the total cost of the drive.

The rotating magnetic levitation system requires muti-axes position information for the levitation control, e.g., 3-translational axes (xyz; x- and y-axes being horizontal and vertical axes, z-axis being orthogonal to both x- and y-axes) and 3-rotational axes around the x, y and z perpendicular axes. Previously developed sensor system provides either translational [3], [5], [7] or rotational axes [8], [9]. Position state feedback for the multi-axis actuator is possible with the combination of sensors which is expensive.

The proposed sensor system provides both horizontal (x) and vertical (y) translational position, and rotary (θ_r rotating around z-axis) position in a single device. Hall-effect sensors are placed radially to measure positions in a single device, therefore, minimizing cost, volume of multi-axis drive system. Rotor horizontal (x) and vertical (y) position offset induced zero-sequence is used; differential information enables translational position estimation in any static rotary angle. No filters that result in phase errors are used in the sensing system. Simple addition and multiplication enable fast and effective rotor translational position and rotary position estimation.

The paper is organized as follows: Hall sensor arrangement is provided in section II; Section III introduces transformation model including zero-sequence components for radial airgap flux; Section IV shows x, y position and the θ_r position sensing algorithm based on zero-sequence; Section V presents the simulation and experimental results; Finally, section VI shows the conclusions.

II. Hall Sensor Arrangement in Airgap

Fig. 1 shows the Hall sensor arrangement from top view with the axes definition of the moving part with magnets, x-y, and θ_r. Twelve hall sensors are placed every $\pi/6$ radially from the center point marked with a red cross. The radial position of hall sensors are defined with mechanical angle, θ_B as summarized in Table I. The moving part consist of four pole permanent magnet (PM). The radial magnetic flux density variation resulted from the x, y, and rotary (θ_r) position displacement are measured by four sets of three-phase hall sensors, abc_n, where n represents the number of three-phase set.

x and y position sensing are possible in any static or dynamic rotary angle position using differential and orthogonal properties; the four sets of three-phase hall sensors will ensure high bandwidth x and y position sensing including zero-angular velocity.

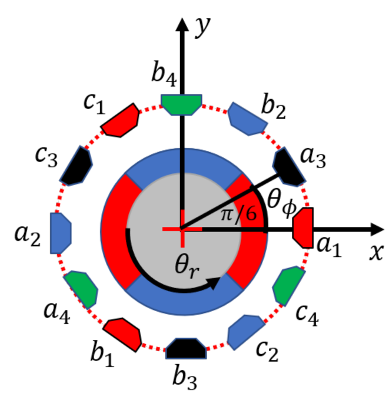

Fig. 1: x-, y-, θ_r-axes and magnetic levitation system and hall sensor arrangement.

.

Table I: Hall sensor mechanical angle, θ_B.

Hall sensor	θ_B [rad]	Hall sensor	θ_B [rad]
a_1	0	a_3	$\pi/6$
b_1	$-2\pi/3$	b_3	$-2\pi/3+\pi/6$
c_1	$2\pi/3$	c_3	$2\pi/3+\pi/6$
a_2	π	a_4	$\pi+\pi/6$
b_2	$\pi-2\pi/3$	b_4	$\pi-2\pi/3+\pi/6$
c_2	$\pi+2\pi/3$	c_4	$\pi+2\pi/3+\pi/6$

III. Off-Centered Rotor and Zero-Sequence

In this section, three-phase airgap field model is provided. The model explains how zero-sequence behaves with respect to each set of hall sensors in Table I at off-centered rotor position in x- and y-axes.

A. $\alpha\beta\gamma_n$-axes and abc_n-axes

Three-phase vector are presented in space vector form (α_n, β_n, γ_n), taking Clark transformation in (1), K_c. α_n and β_n are orthogonal components in stationary reference frame. γ_n is the zero-sequence that exist only when abc_n are not in balance. In Fig. 2, $\alpha\beta_n$ axes and corresponding three-phase hall sensor axes, abc_n, are shown. Note that the $\alpha\beta_2$ in Fig. 2 (a) is phase shifted π mechanically from $\alpha\beta_1$; the x- and y-axis for the $\alpha\beta_1$ and $\alpha\beta_2$ are mirrored. The two sets of space vector are intentionally arranged in this way to use differential information to cancel out the higher order harmonic flux components. Similarly, $\alpha\beta_3$ and $\alpha\beta_4$ shown in Fig. 2 (b) are placed in mirrored position. $\alpha\beta_3$ and $\alpha\beta_4$ are $\pi/6$ shifted mechanically from $\alpha\beta_1$ and $\alpha\beta_2$ to result in orthogonal differential information. This enables x and y position measurement in any static or dynamic rotary angular movement, θ_r.

$$\begin{bmatrix}\alpha_n\\ \beta_n\\ \gamma_n\end{bmatrix} = \frac{2}{3}\begin{bmatrix}1 & \text{-0.5} & \text{-0.5}\\ 0 & \frac{\sqrt{3}}{2} & -\frac{\sqrt{3}}{2}\\ \frac{1}{2} & \frac{1}{2} & \frac{1}{2}\end{bmatrix}\begin{bmatrix}a_n\\ b_n\\ c_n\end{bmatrix} = K_c\begin{bmatrix}a_n\\ b_n\\ c_n\end{bmatrix} \quad (1)$$

B. Radial airgap field modeling

Rotating radial airgap field is modeled using Euler's formula. The airgap flux density measured by hall sensor is inversely proportional to the airgap distance. The number of pole pair of moving part, p, is equal to 2. The radial airgap field of each hall sensor in Table I is modeled taking the following three steps shown in Fig. 3 (a), (b), and (c), respectively: (a) Calculating the relative airgap radius , r' and (2) and the relative offset angle, $\Delta\theta$, using (3) in translational position offset in x and y direction, Δx and Δy ; (b) Calculating the airgap field using (4) in x and y direction, $B_{mx}+jB_{my}$, by taking rotating transform the airgap field with new airgap radius; (c) Extracting radial airgap field by taking real component after rotating transform as in (5). Fig. 3 is showing the example vector diagram when the rotor offset in y-axis, Δy, for a_1 which is denoted by a_1'. For different hall sensor, corresponding θ_B in Table I should be used.

$$r' = |r - (\Delta x + j\Delta y)\ exp(j\theta_B)| \quad (2)$$

$$\Delta\theta = \angle(r - (\Delta x + j\Delta y)\ exp(j\theta_B)) \quad (3)$$

$$(B_{mx} + jB_{my}) = \frac{1}{r'}\ exp(\text{-}j\theta_r)\ exp(jp(\theta_B - \Delta\theta)) \quad (4)$$

$$B_{m\theta} = real((B_{mx} + jB_{my})\ exp(j\Delta\theta)) \quad (5)$$

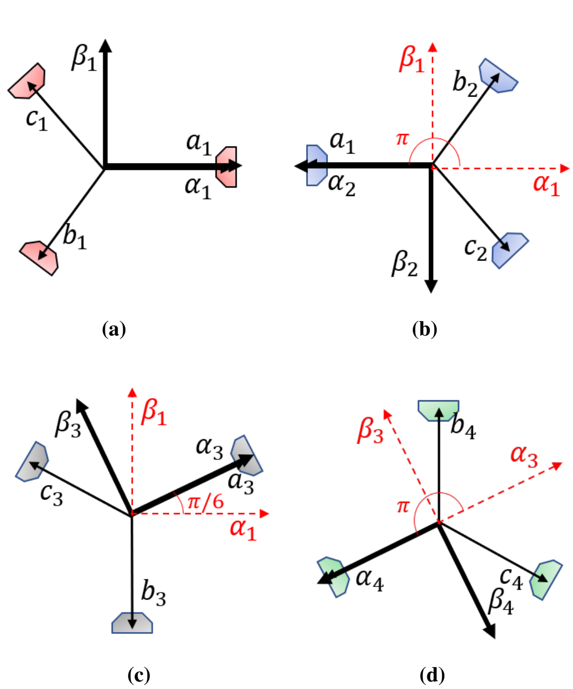

Fig. 2: Three-phase hall sensor placement and the Clark-transformed axis. (a) abc_1-axes and $\alpha\beta_1$-axes. (b) abc_2-axes and $\alpha\beta_2$-axes. (c) abc_3-axes and $\alpha\beta_3$-axes. (d) abc_4-axes and $\alpha\beta_4$-axes.

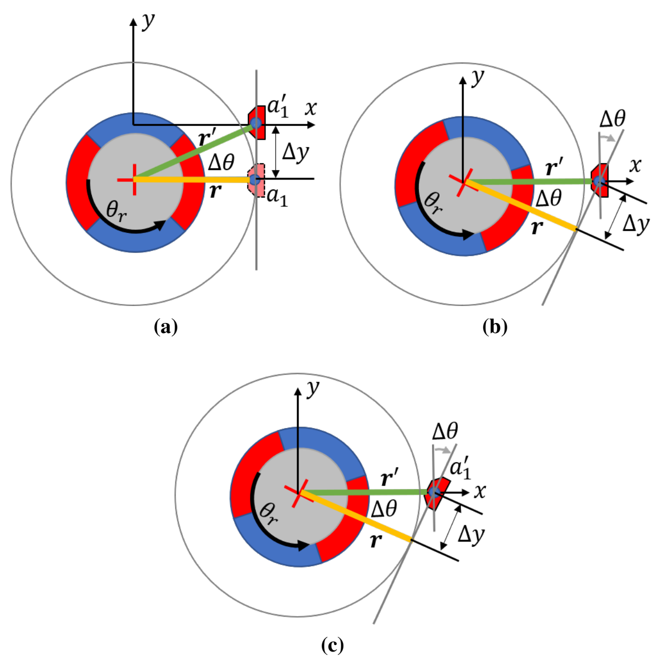

Fig. 3: Hall sensor radial field calculation example for a_1 with Δy. (a) Relative airgap radius, r' and offset angle, $\Delta\theta$, at a_1'. (b) Airgap field calculation at a_1'. (c) Radial airgap field calculation.

C. Rotor position offset effect on α_n, β_n, γ_n

Offset Δx and Δy effect on α_n, β_n, γ_n are calculated for four sets of three-phase based on trigonometric function.The first three-phase input with the position offset, o_{xy1}, in (6) is shown in (7). α_1, β_1, and γ_1 are calculated in (8)-(10) using (1). Note that the o_{xy} effect on α_1 and β_1 canceled out where as the magnitude of zero-sequence, γ_1 become non-zero and is proportional to the Δx and Δy (10). Zero-sequence does not exist when rotor is rotating at the centered position, i.e., Δx=0, Δy=0. The phase offset of zero-sequence is atan(Δy / Δx) (10).

$$o_{xy1} = \Delta x\ cos(\theta_r) + \Delta y\ sin(\theta_r) \tag{6}$$

$$\begin{bmatrix} a_1 \\ b_1 \\ c_1 \end{bmatrix} = \begin{bmatrix} cos(\theta_r) + o_{xy1} \\ cos(\theta_r - \frac{2\pi}{3}) + o_{xy1} \\ cos(\theta_r + \frac{2\pi}{3}) + o_{xy1} \end{bmatrix} \tag{7}$$

$$\begin{aligned} \alpha_1 &= \frac{2}{3}\left[cos(\theta_r) - \frac{cos(\theta_r - \frac{2\pi}{3})}{2} - \frac{cos(\theta_r + \frac{2\pi}{3})}{2}\right] \\ &= cos(\theta_r) \end{aligned} \tag{8}$$

$$\begin{aligned} \beta_1 &= \frac{2}{3}\left[\frac{\sqrt{3}}{2}cos(\theta_r - \frac{2\pi}{3}) - \frac{\sqrt{3}}{2}cos(\theta_r + \frac{2\pi}{3})\right] \\ &= sin(\theta_r) \end{aligned} \tag{9}$$

$$\begin{aligned} \gamma_1 &= \Delta x\ cos(\theta_r) + \Delta y\ sin(\theta_r) \\ &= \sqrt{\Delta x^2 + \Delta y^2}\ cos\left(\theta_r - atan(\frac{\Delta y}{\Delta x})\right) \end{aligned} \tag{10}$$

α_2, β_2, and γ_2 are calculated using the same procedure. The magnitude and phase for α_2, β_2 in (11) and (12) are the same for α_1, β_1 since the effect of the position offset is canceled. The magnitude γ_2 in (13) and γ_1 in (10) are the same. However, the phase of γ_2 is shifted π, the zero-sequence exist in opposite direction. The Δx and Δy have mirrored effect for γ_2 as shown in Fig. 4.

$$\alpha_2 = cos(\theta_r) \tag{11}$$

$$\beta_2 = sin(\theta_r) \tag{12}$$

$$\gamma_2 = \sqrt{\Delta x^2 + \Delta y^2}\ cos\left(\theta_r + \pi - atan(\frac{\Delta y}{\Delta x})\right) \tag{13}$$

Fig. 4 shows α, β, γ phasor components for $\alpha\beta 1$ and $\alpha\beta 2$ with x-axis offset, Δx. Δy is zero. o_1 and o_1' are absolute center position and new center position with offset Δx. Fig. 4 (a) and (b) are the phasors at θ_r=0 and (b) and (c) are the phasors at θ_r=$\pi/2$. The Δx effect on $\alpha\beta 1$ and $\alpha\beta 2$ at o_1' are in opposite direction since $\alpha\beta 1$ and $\alpha\beta 2$ are mechanically placed with π angular offset.

Fig. 5 (a) shows the radial field results calculated using (2)-(5) with Δ_x of 0.1p.u. Fig. 5 (b) shows the Clark transformed results. The phase of $B_{\gamma 1}$ and $B_{\gamma 2}$ are π shifted. This mirrored zero-sequence property is important to enable the estimation of x and y position sensing using differential information.

α_3, β_3, and γ_3 are modeled in (14)-(18) and α_4, β_4, and γ_4 are modeled in (19)-(21) following the same procedure. Fig. 5 (c) shows the radial field results of B_{abc3} and B_{abc4} calculated

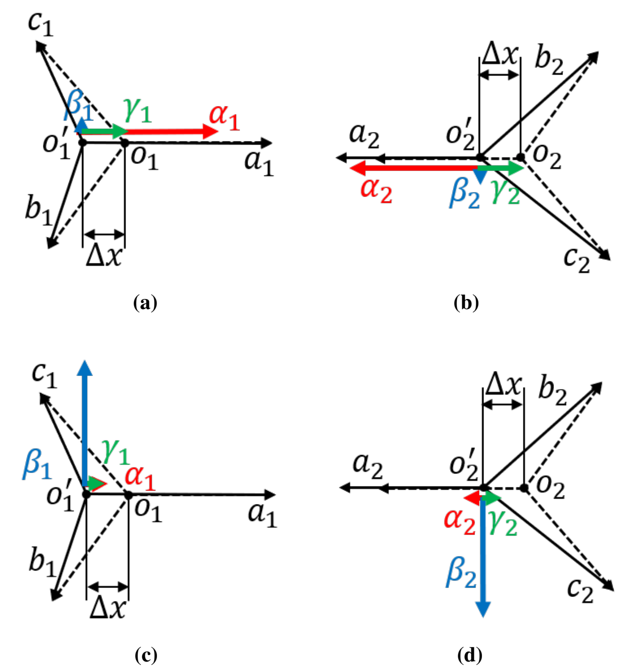

Fig. 4: (a) α_1, β_1, γ_1 at θ_r=0. (b) α_2, β_2, γ_2 at θ_r=0. (c) α_1, β_1, γ_1 at θ_r=$\pi/2$. (d) α_2, β_2, γ_2 at θ_r=$\pi/2$.

using (2)-(5) with Δx of 0.1p.u. Fig. 5 (d) shows the Clark transformed results. The phase of $B_{\gamma 3}$ and $B_{\gamma 4}$ are π shifted.

$$\begin{aligned} o_{xy3} = \Delta x\ cos&\left((\theta_r + p\frac{\pi}{6}) + \frac{\pi}{6}\right) \\ &+ \Delta y\ sin\left((\theta_r + p\frac{\pi}{6}) + \frac{\pi}{6}\right) \end{aligned} \tag{14}$$

$$\begin{bmatrix} a_3 \\ b_3 \\ c_3 \end{bmatrix} = \begin{bmatrix} cos(\theta_r - p\frac{\pi}{6}) + o_{xy3} \\ cos(\theta_r - \frac{2\pi}{3} - p\frac{\pi}{6}) + o_{xy3} \\ cos(\theta_r + \frac{2\pi}{3} - p\frac{\pi}{6}) + o_{xy3} \end{bmatrix} \tag{15}$$

$$\alpha_3 = cos(\theta_r - \frac{\pi}{3}) \tag{16}$$

$$\beta_3 = sin(\theta_r - \frac{\pi}{3}) \tag{17}$$

$$\gamma_3 = \sqrt{\Delta x^2 + \Delta y^2}\ cos\left(\theta_r - \frac{\pi}{2} - atan(\frac{\Delta y}{\Delta x})\right) \tag{18}$$

$$\alpha_4 = cos(\theta_r - \frac{\pi}{3}) \tag{19}$$

$$\beta_4 = sin(\theta_r - \frac{\pi}{3}) \tag{20}$$

$$\gamma_4 = \sqrt{\Delta x^2 + \Delta y^2}\ cos\left(\theta_r + \frac{\pi}{2} - atan(\frac{\Delta y}{\Delta x})\right) \tag{21}$$

IV. Rotor Position Estimation

In this section, the translational rotor position, x and y, and rotary position, θ_r estimation algorithm is explained. The post-processing of magnetic field to estimate the rotor positions are shown in detail.

A. Translational Position Estimation

It has been investigated that the magnitude and the phase of zero-sequence are proportion to magnitude and the ratio of

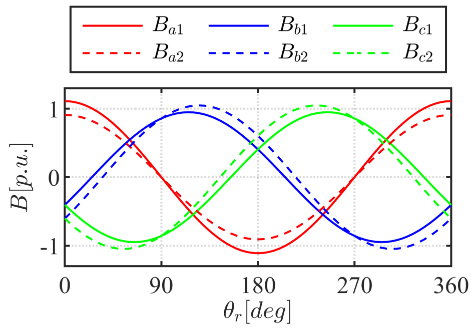

(a)

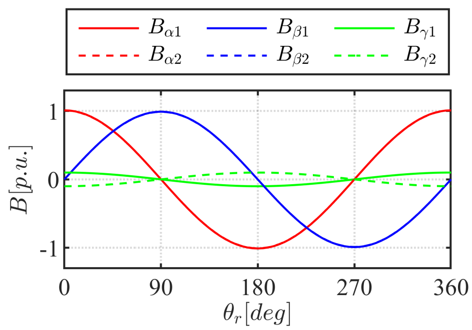

(b)

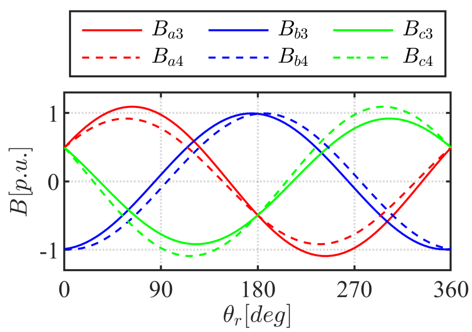

(c)

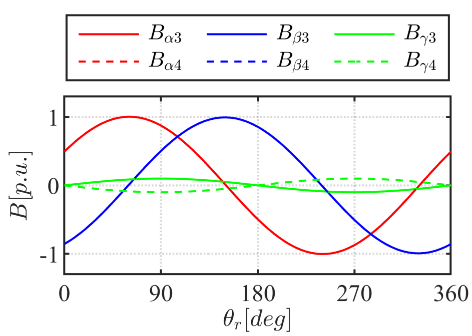

(d)

Fig. 5: Airgap field results with Δx=0.1p.u Δy=0 over one electrical period. (a) B_{abc1} and B_{abc2} phase flux density. (b) $B_{\alpha\beta\gamma1}$ and $B_{\alpha\beta\gamma2}$. (c) B_{abc3} and B_{abc4} phase flux density. (d) $B_{\alpha\beta\gamma3}$ and $B_{\alpha\beta\gamma4}$.

Δx and Δy. Extracting the zero-sequence will enable Δx and Δy measurement.

In (22), differential zero-sequence, x_{12} and y_{12}, are extracted by multiplying the zero-sequence, $\alpha_1\gamma_1$ with $_1$ and $\beta_1\gamma_1$ and subtract the mirrored components $\alpha_2\gamma_2$ and $\beta_2\gamma_2$. Using the differential information, the higher-order harmonic components effects are zeroed.

Similarly, x_{34} and y_{34} are calculated in (23). Since the abc_3 and abc_4 are $\pi/6$ mechanically shifted from abc_1 and abc_2 as in Fig. 2, the x_{34} and y_{34} are rotated back using rotating transform in (23). Fig. 6 (a) shows the x_{12}, x_{34} and y_{12}, y_{34} over one electrical period. The phase difference between x_{12}, x_{34} and y_{12}, y_{34} are π.

$$\begin{aligned}\begin{bmatrix} x_{12} \\ y_{12} \end{bmatrix} &= \begin{bmatrix} \alpha_1\gamma_1 - \alpha_2\gamma_2 \\ \beta_1\gamma_1 - \beta_2\gamma_2 \end{bmatrix} \\ &= \begin{bmatrix} \Delta x + \Delta y\ sin(2\theta_r) + \Delta x\ cos(2\theta_r) \\ \Delta y + \Delta x\ sin(2\theta_r) - \Delta y\ cos(2\theta_r) \end{bmatrix}\end{aligned} \tag{22}$$

$$\begin{aligned}\begin{bmatrix} x_{34} \\ y_{34} \end{bmatrix} &= \begin{bmatrix} cos(\frac{-\pi}{6}) & -sin(\frac{-\pi}{6}) \\ sin(\frac{-\pi}{6}) & cos(\frac{-\pi}{6}) \end{bmatrix} \begin{bmatrix} \alpha_3\gamma_3 - \alpha_4\gamma_4 \\ \beta_3\gamma_3 - \beta_4\gamma_4 \end{bmatrix} \\ &= \begin{bmatrix} \Delta x - \Delta y\ sin(2\theta_r) - \Delta x\ cos(2\theta_r) \\ \Delta y - \Delta x\ sin(2\theta_r) + \Delta y\ cos(2\theta_r) \end{bmatrix}\end{aligned} \tag{23}$$

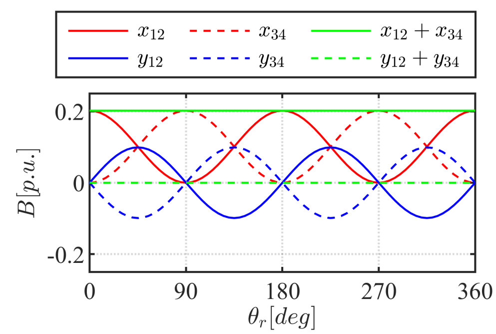

(a)

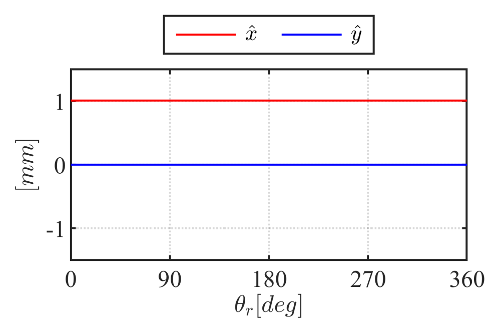

(b)

Fig. 6: (a) x_{12}, x_{34} and y_{12}, y_{34}, Δx=0.1p.u Δy=0.. (b) Estimated translational position, $\hat{x}$ and $\hat{y}$, Δx=0.1p.u Δy=0.

Finally, by summing the (22) and (23), x and y position are estimated in (24) where k_g is the gain for unit conversion from flux density to position unit, i.e., millimeter. It is interesting to note that the proposed position sensing method is not rotor position dependant at any instance; the x and y position is measured regardless of rotary position, θ_r. No filter that can result in phase delay is used. Simple addition and multiplication are used to enable fast and effective rotor translational position estimation.

$$\begin{bmatrix} \hat{x} \\ \hat{y} \end{bmatrix} = k_g \begin{bmatrix} x_{12} + x_{34} \\ y_{12} + y_{34} \end{bmatrix} = k_g \begin{bmatrix} 2\Delta x \\ 2\Delta y \end{bmatrix} \tag{24}$$

B. Rotary angle Estimation

θ_r position is estimated using arc tangent. Taking Clark transform, α_n and β_n are calculated. Higher order harmonic degrades the phase estimation result. The accuracy of rotor angular position is enhanced using differential information between $\alpha\beta_1$ and $\alpha\beta_2$. Averaging $\hat{\theta}_1$ (25) and $\hat{\theta}_2$ (26), rotor electrical angle is estimated (27). To convert electrical angle to mechanical angle, the number of pole pair is multiplied (28).

$$\theta_1 = atan2(B_{\beta 2}, B_{\alpha 1}) \tag{25}$$

$$\theta_2 = atan2(B_{\beta 1}, B_{\alpha 2}) \tag{26}$$

$$\hat{\theta}_r = \frac{\theta_1 + \theta_2}{2} \tag{27}$$

$$\hat{\theta}_m = \frac{\hat{\theta}_r}{p} \tag{28}$$

C. Implementation

Fig. 7 shows block diagram of x and y position estimation and θ_r estimation. 9-multiplication and 3-addition are required for Clark transformation in (1) and 4-multiplication and 2-addition are required for rotating transformation. Therefore, 50-multiplication and 32-addition are required every calculation period for $\hat{x}$ and $\hat{y}$. No memory is required since the signal processing does not include filtering process. Also, the translational position estimation process is independent of the rotary position information. This implies that the algorithm assures consistent performance in any static rotor position regardless of the sampling frequency of discrete domain implementation.

V. Simulation and Experimental results

Proposed sensing algorithm is verified with Finite element analysis (FEA) simulation and experimentation.

A. Simulation Results

1) Translational position sensing results: 2-dimensional FEA simulation is performed. Fig. 8 shows the FEA model geometry and flux density measured positions where D_{hall}, D_{ri}, and t_{PM} represent the diameter of hall sensors, diameter of the rotor shaft, and PM thickness. Table II includes the simulation conditions. – These can be changed matching with the test device in the experimentation later.

Table II: FE analysis conditions

Pole pairs, p	2	D_{ri}	10 [mm]
Permanent magnet	N35	D_{hall}	15 [mm]
Shaft material	M-19	t_{PM}	1.5 [mm]
x_{max}	± 1.5 [mm]	L_{st}	5 [mm]
y_{max}	± 1.5 [mm]		

Fig. 9 (a) shows the phase flux density FEA results of abc_1 and abc_2 at x=1mm, y=0mm while rotating 0 to 2π. Taking Clark transform, the $\alpha\beta_1$ and $\alpha\beta_2$ are shown in Fig. 9 (b)

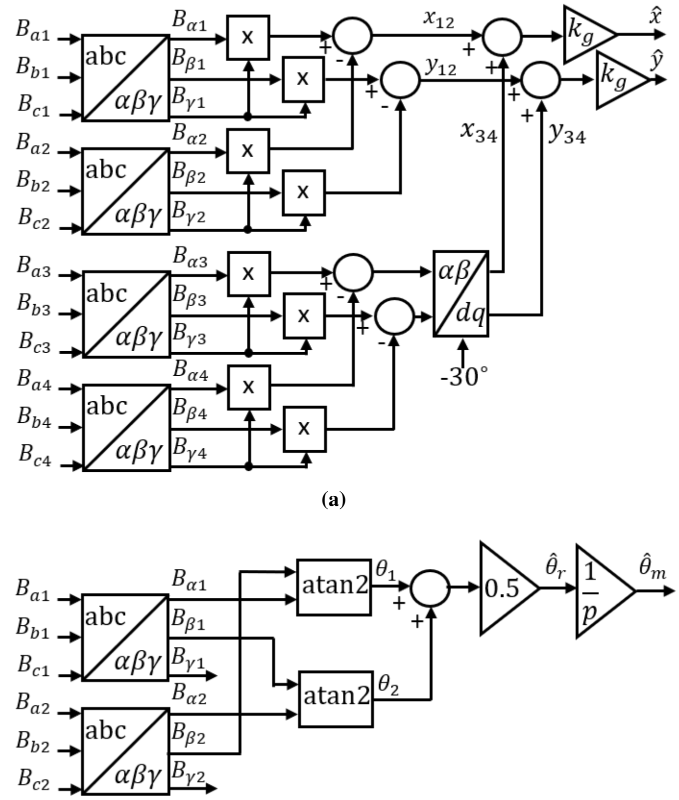

Fig. 7: (a) Translational position estimation block diagram. (b) Rotary position estimation block diagram.

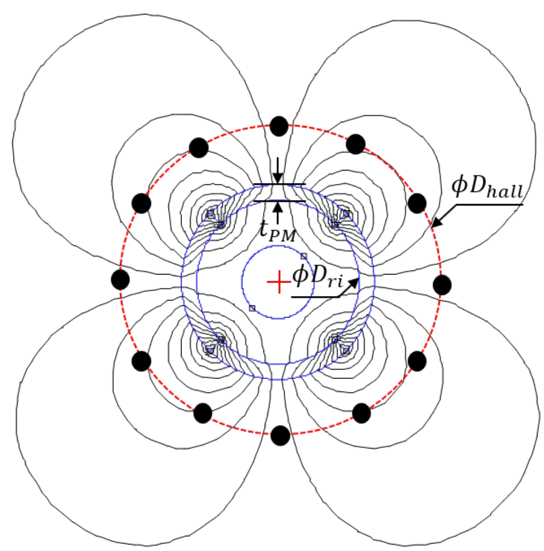

Fig. 8: FEA simulation geometry.

with zero-sequence. It can be observed that α_1 is larger than α_2 since the PM is placed at x=1mm.

Fig. 10 (a) shows the of $\alpha\beta_1$ and $\alpha\beta_2$ at x=1mm and y=0mm over θ_r= 0 to 2π. The differential components which contains x and y position information, x_{12}, y_{12}, y_{34}, and y_{34}, are calculated using (22) and (23). Note that the mean value of x_{12}, y_{12}, x_{34}, and y_{34} are proportional to the xy position, but rotor position dependant. To enable xy position estimation in any static rotor position x_{12} and x_{34} are summed; y_{12} and y_{34} are summed (24) as shown in Fig. 10 (b).

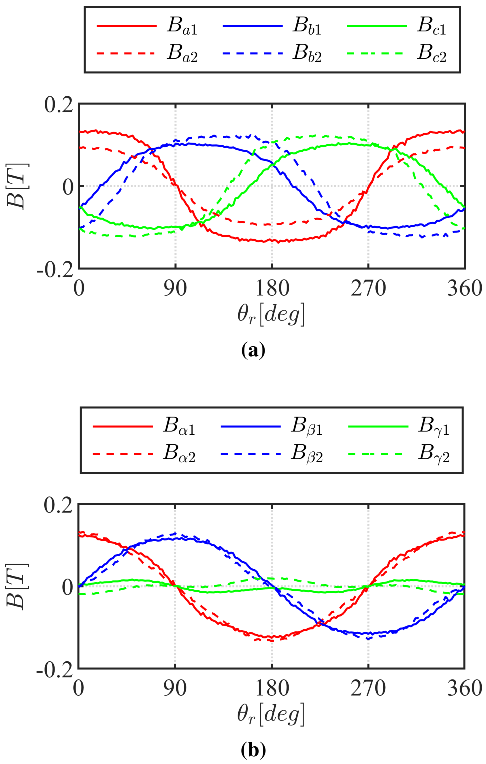

Fig. 9: FEA simulation results in θ_r from 0 to 360 degree. (a) abc_1 and abc_2 phase flux density. (b) Clark transformed flux density, $\alpha\beta1$ and $\alpha\beta2$

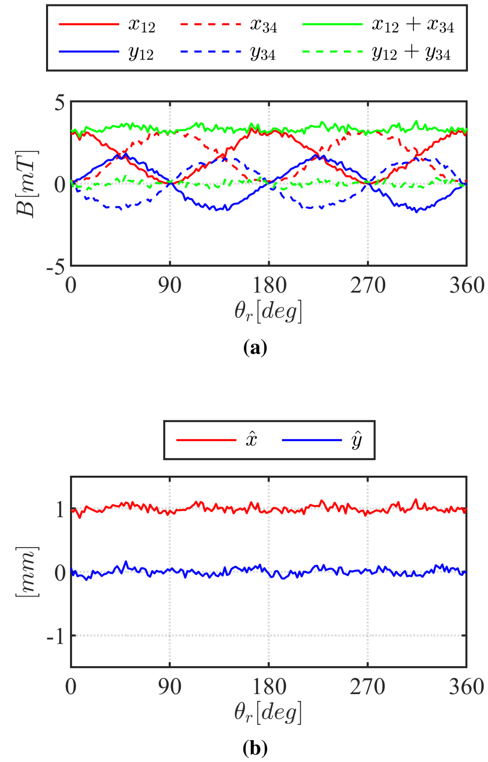

Fig. 10: FEA simulation results in θ_r from 0 to 360 degree. (a) x_{12}, x_{34}, y_{12}, y_{34} from four sets of three-phase hall sensors. (b) Estimated translational position, $\hat{x}$ and $\hat{y}$.

Finally, Fig. 11 shows estimated x and y position in x=[-1:0.5:1]mm and y=[-1:0.5:1]mm while rotor rotates from 0 to 2π.

2) Rotary angle sensing results: Fig. 12 shows the phase estimation results from (25), (26), and (27). Fig. 12 (a) shows the overlapped phase results from $\alpha\beta_1$ and $\alpha\beta_2$. Fig. 12 (b) shows error.

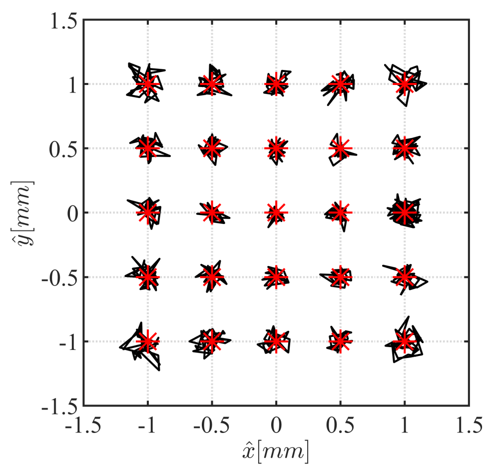

Fig. 11: Estimated $\hat{x}$ and $\hat{y}$ position (black) and actual rotor position (red) while rotor rotating in one full electrical angle.

B. Experimental results

VI. Conclusions

The proposed x-, y-, θ_r-position sensor is xxx. Experimental results have been provided to support the viability of the proposed technique. No filters that result in phase errors are used. Simple addition and multiplication are used to enable fast and effective rotor translational position and rotary position estimation.

References

[1] A. Chiba, T. Fukao, O. Ichikawa, M. Oshima, M. Takemoto, and D. G. Dorrell, *Magnetic bearings and bearingless drives*. Elsevier, 2005.

[2] H. Sugimoto and A. Chiba, "Parameter identification of current–force factor and torque constant in single-drive bearingless motors with back emf," *IEEE Transactions on Industry Applications*, vol. 55, no. 5, pp. 4754–4761, 2019.

[3] S. Yang and C. Huang, "A hall sensor-based three-dimensional displacement measurement system for miniature magnetically levitated rotor," *IEEE Sensors Journal*, vol. 9, no. 12, pp. 1872–1878, 2009.

[4] M. Noh, W. Gruber, and D. L. Trumper, "Hysteresis bearingless slice motors with homopolar flux-biasing," *IEEE/ASME Transactions on Mechatronics*, vol. 22, no. 5, pp. 2308–2318, 2017.

[5] C. Elbuken, M. B. Khamesee, and M. Yavuz, "Design and implementation of a micromanipulation system using a magnetically levitated mems robot," *IEEE/ASME Transactions on Mechatronics*, vol. 14, no. 4, pp. 434–445, 2009.

[6] W. Amrhein, W. Gruber, W. Bauer, and M. Reisinger, "Magnetic levitation systems for cost-sensitive applications—some design aspects," *IEEE Transactions on Industry Applications*, vol. 52, no. 5, pp. 3739–3752, 2016.

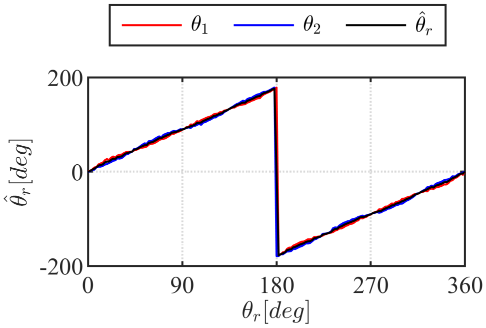

(a)

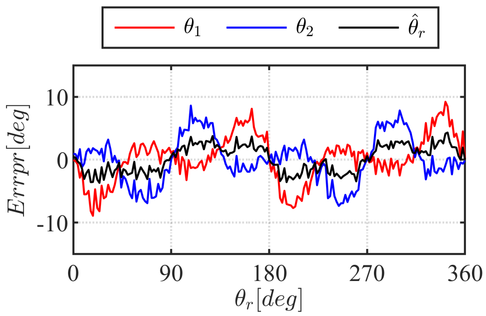

(b)

Fig. 12: (a) Estimated rotary position, $\hat{\theta}_r$. (b) Rotary position estimation error.

[7] X. Zhang, M. Mehrtash, and M. B. Khamesee, “Dual-axial motion control of a magnetic levitation system using hall-effect sensors,” *IEEE/ASME Transactions on Mechatronics*, vol. 21, no. 2, pp. 1129–1139, 2016.

[8] Y. G. Kang, D. F. Laborda, D. Fernández, D. Reigosa, and F. Briz, “Magnetic resolver using hall-effect sensors,” in *2020 IEEE Energy Conversion Congress and Exposition (ECCE)*, 2020, pp. 2344–2350.

[9] D. Fernandez, D. Fernandez, M. Martinez, D. Reigosa, A. B. Diez, and F. Briz, “Resolver emulation for pmsms using low cost hall-effect sensors,” *IEEE Transactions on Industry Applications*, vol. 56, no. 5, pp. 4977–4985, 2020.